

Alma Mater Studiorum Università di Bologna  
Archivio istituzionale della ricerca

Global and local characterization explains the different mechanisms of failure of the human ribs

This is the final peer-reviewed author's accepted manuscript (postprint) of the following publication:

*Published Version:*

Palanca M., Liebsch C., Hubner S., Marras D., Ruspi M.L., Marconi F., et al. (2022). Global and local characterization explains the different mechanisms of failure of the human ribs. JOURNAL OF THE MECHANICAL BEHAVIOR OF BIOMEDICAL MATERIALS, 125, 1-9 [10.1016/j.jmbbm.2021.104931].

*Availability:*

This version is available at: <https://hdl.handle.net/11585/841838> since: 2021-12-15

*Published:*

DOI: <http://doi.org/10.1016/j.jmbbm.2021.104931>

*Terms of use:*

Some rights reserved. The terms and conditions for the reuse of this version of the manuscript are specified in the publishing policy. For all terms of use and more information see the publisher's website.

This item was downloaded from IRIS Università di Bologna (<https://cris.unibo.it/>).  
When citing, please refer to the published version.

(Article begins on next page)

This is the final peer-reviewed accepted manuscript of:

**Global and local characterization explains the different mechanisms of failure of the human ribs.**

**Palanca M, Liebsch C, Hübner S, Marras D, Ruspi ML, Marconi F, Cristofolini L, Wilke HJ.**

**J Mech Behav Biomed Mater. 2022 Jan;125:104931.**

**doi: 10.1016/j.jmbbm.2021.104931. Epub 2021 Oct 28.**

The final published version is available online at:

<https://doi.org/10.1016/j.jmbbm.2021.104931>

<https://www.sciencedirect.com/science/article/pii/S1751616121005622>

Rights / License:

The terms and conditions for the reuse of this version of the manuscript are specified in the publishing policy. For all terms of use and more information see the publisher's website.

*This item was downloaded from IRIS Università di Bologna (<https://cris.unibo.it/>)*

***When citing, please refer to the published version.***

# Global and local characterization explains the different mechanisms of failure of the human ribs

Marco Palanca<sup>1,2,3</sup>, Christian Liebsch<sup>4</sup>, Shamila Hübner<sup>4</sup>,  
Daniele Marras<sup>3</sup>, Maria Luisa Ruspi<sup>3</sup>, Francesco Marconi<sup>3</sup>,  
Luca Cristofolini<sup>3\*</sup>, Hans-Joachim Wilke<sup>4</sup>

LC and H-J W share the co-senior authorship

<sup>1</sup> Department of Oncology and Metabolism, University of Sheffield, Sheffield, UK

<sup>2</sup> INSIGNEO Institute for in silico medicine, University of Sheffield, Sheffield, UK

<sup>3</sup> Department of Industrial Engineering, Alma Mater Studiorum – Università di Bologna, Bologna, Italy

<sup>4</sup> Institute of Orthopaedic Research and Biomechanics, Trauma Research Center Ulm (ZTF), University Hospital Ulm, Ulm, Germany

\*Corresponding author:

*Email: luca.cristofolini@unibo.it*

Department of Industrial Engineering, Alma Mater Studiorum – Università di Bologna, Via Umberto Terracini 24-28, 40131 Bologna, Italy

# 1 Abstract

2 Knowledge of the mechanics and mechanistic reasons inducing rib fracture is fundamental for  
3 forensic investigations and for the design of implants and cardiopulmonary resuscitation devices.  
4 A mechanical rationale to explain the different rib mechanisms of failure is still a challenge. The aim  
5 of this work was to experimentally characterize human ribs to test the hypothesis that a correlation  
6 exists between the ribs properties and the mechanism of failure. 89 ribs were tested in antero-  
7 posterior compression. The full-field strain distribution was measured through Digital Image  
8 Correlation. The fracture load ranged 7 - 132 N. Two main different mechanisms of failure were  
9 observed: brittle and buckling. The strain analysis showed that the direction of principal strains was  
10 either aligned with the ribs, or oblique, around 45°, with a rather uniform direction in the most  
11 strained area. The maximum principal strains were in the range between 1000 and 30000  
12 microstrain and the minimum principal strain between -30000 and -800 microstrain. The ribs  
13 undergoing brittle fracture had significantly thicker cortical bone than those undergoing buckling.  
14 Also, larger tensile strains were observed in the specimens with brittle fracture than in the buckling  
15 ones. These findings support the focus of cortical thickness modelling which could help in  
16 sharpening computational models for the aforesaid purposes.

## 17 Keywords:

18 human ribs, in vitro biomechanical tests, mechanism of failure, fracture pattern, strain analysis,  
19 digital image correlation

## 20 Introduction

21 Rib fractures occur within a wide range of accident types. These accidents include falls or collisions  
22 which involve blunt chest trauma, or are the unwanted side-effect of emergency operations, (e.g.  
23 cardiopulmonary resuscitation), or are the result of traffic accidents (Brasel et al., 2006; Duma et  
24 al., 2011; Liebsch et al., 2019b; Nirula and Mayberry, 2010). Due to the high incidence of rib  
25 fractures and the associated high rates of mortality and morbidity (Kent et al., 2008), deformability  
26 and fragility of the ribs is studied by the scientific community from various perspectives (Kang et al.,  
27 2021; Liebsch and Wilke, 2018; Pezowicz and Glowacki, 2021). A better understanding of the  
28 mechanical behaviour of the ribs would be important for basic science (e.g.: improve the modelling  
29 strategy) but also for clinical purposes. In fact, a deep knowledge of the mechanical behavior of the  
30 ribs could aid in the design of better safety devices and improve the reconstruction of traumatic  
31 events in the forensic field (Campbell et al., 2009; Daegling et al., 2008; Kang et al., 2021; Mohr et  
32 al., 2007).

33 *In vitro* experiments were performed to characterize ribs mechanical behaviour and their fracture  
34 mechanism. Three-point bending and antero-posterior compression tests were used to characterize  
35 the material properties as well as the structural biomechanical response of ribs (Harden et al., 2019;  
36 Iraeus et al., 2020; Li et al., 2010a; Liebsch et al., 2021; Love and Symes, 2004; Pezowicz and  
37 Glowacki, 2021; Yoganandan and Pintar, 1998). Moreover, subject-specific anatomical and  
38 morphological factors, such as the rib level, the cortical thickness and the bone mineral density,  
39 were found to play a fundamental role for the fragility of the ribs, and thus for the prediction of  
40 possible failures (Harden et al., 2019; Holcombe et al., 2019, 2018; Kemper et al., 2007; Liebsch et  
41 al., 2021). By contrast, age, sex, and height were found to play minor roles in rib fragility (Harden  
42 et al., 2017; Liebsch et al., 2021).

43 More complex is the definition of the fracture patterns and of the mechanisms of failure. A first  
44 analysis and classification of the fracture patterns was performed in a retrospective study with  
45 almost 500 ribs, mostly harvested during autopsy (Love and Symes, 2004). This study, with a forensic  
46 motivation, described four patterns of fracture (transverse, oblique, butterfly, and buckle) and  
47 showed the lack of systematic correlation with age, sex, and ancestry. Moreover, the authors clearly  
48 underlined how the ribs' failure point seemed to contradict the bone biomechanics literature.  
49 Indeed, it is well known that bone is stronger in compression and weaker in tension (Bayraktar et  
50 al., 2004; Keaveny et al., 1994; Reilly and Burstein, 1975). However, (Love and Symes, 2004)  
51 repeatedly observed failures at the points of compression prior to points of tension. The same

52 clinically relevant fracture patterns were replicated *in vitro* (Daegling et al., 2008; Harden et al.,  
53 2019), where fracture loads and point-wise strains, using strain gauges, were measured. While the  
54 tests simulated clinically relevant fracture of the ribs, a mechanistic rationale to explain the different  
55 patterns of fracture was not outlined.

56 The work of Love and Symes (2004) also identified two possible mechanisms of failure: brittle and  
57 buckling. While elderly bones (more brittle) are less likely to exhibit plastic response to loading, a  
58 high-strain (buckling) failure is expected in young bones (Agnew et al., 2014). However, rib  
59 properties that preliminary indicate which mechanisms of failure could be expected have not yet  
60 been identified.

61 Finite element models were developed to better understand rib responses to different impact loads  
62 together with the growing experimental biomechanical knowledge. In fact, the great amount of  
63 experimental data allowed to generate more biofidelic models and to refine their prediction. Both  
64 in generic (Iraeus et al., 2020; Wang et al., 2016) and subject-specific (Iraeus et al., 2019; Li et al.,  
65 2010a, 2010b) finite element models, the predicted fracture load, stiffness, and strain values were  
66 validated against experimental data. However, the prediction of the fracture onset location and the  
67 mechanisms of failure remain a challenge.

68 In this context, a study that matches anatomical and morphometric details with a comprehensive  
69 biomechanical characterization of the strain field to describe the possible cause-effect relations is  
70 still missing.

71 This study provides a comprehensive characterization of human ribs in terms of global behaviour of  
72 the different ribs (e.g. failure load, rib level), and of local properties (e.g. strain pattern, and cortical  
73 thickness at the location of fracture onset). Therefore, the purpose of this study was to test the  
74 hypothesis that the global behaviour and local properties explain the mechanism of failure.

## 75 Material and methods

### 76 Sample preparation

77 The same sample that was used in the study of (Liebsch et al., 2021) to identify the anthropometric  
78 factors that promote rib fragility was used in the present study. The sample consisted of 89 fresh  
79 frozen ribs from 13 donors, from levels 4 to 8 (Table 1). Specimens were obtained through an  
80 ethically-approved donation program; the entire study was approved by the ethics committee of  
81 the University of Ulm (vote no. 92/20).

82 The ribs were isolated from the spines (vertebral extremity) by carefully cutting the ligaments and  
 83 removing the muscles, and anteriorly (sternal extremity) by cutting the costal cartilage. The  
 84 periosteum was removed using fine sandpaper, taking care not to damage the periosteal cortical  
 85 shell. The vertebral and sternal extremities of the ribs were embedded in poly-methyl-methacrylate  
 86 (Technovit 3040, Heraeus Kulzer, Germany) for a length of about 40 mm to guarantee a stable  
 87 fixation with the testing setup. The ribs were frozen in sealed bags when not in use and thawed the  
 88 night before the test in physiological saline solution.

89 Before the tests, rib surfaces were sprayed with a thin layer of white water-based paint and then  
 90 with a black random speckle pattern (Lionello and Cristofolini, 2014; Palanca et al., 2015) to allow  
 91 Digital Image Correlation (DIC) measuring the strains.

92 *Table 1: Summary of the donors' details and ribs tested. The letter "C" indicates that the strain analysis was*  
 93 *performed on the cutaneous surface; "P" on the pleural surface.*

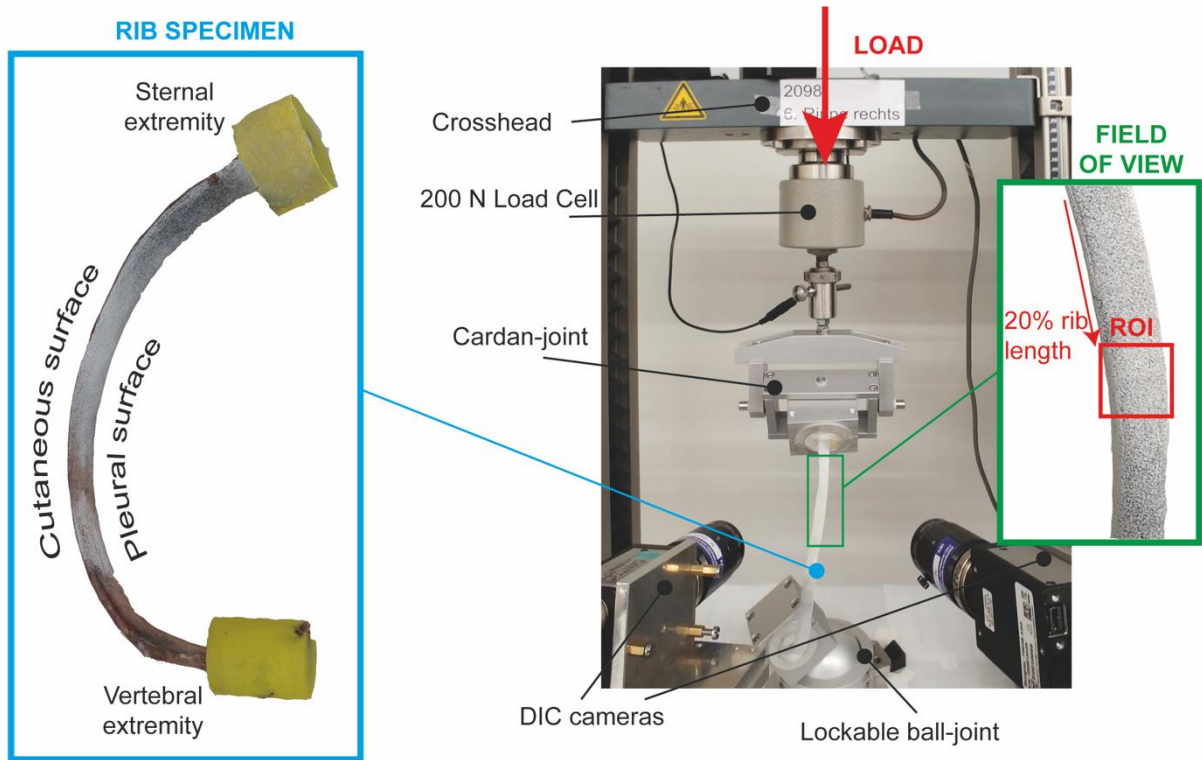
Donor	Age (y)	Sex	Rib level									
			Right					Left				
			4	5	6	7	8	4	5	6	7	8
1	55	F					P					C
2	62	M	C	P	C	P	C	P	C	P	C	P
3	63	M	P	C		P	C	C	P		C	P
4	64	F				C	P			C	P	C
5	65	F							C	P		C
6	68	M	P	C	P	C	P	C	P	C	P	C
7	71	F		P		P	P	P	C		P	C
8	80	M	P	C	P*	C	P	C	P	C*	P	C
9	81	M	C*	P		P	P	C*	P		C	C
10	84	F	C	P	C	P	C*	P	C	P	C	
11	91	M	P	C		C	P	P	C			
12	96	M	P*	C		P	C	C	P		C	P
13	99	F	P			C					C	

94 \* no DIC data available

## 95 Biomechanical testing

96 A uniaxial testing machine (Z010, Zwick Roell AG, Germany) equipped with a 200 N load cell was  
 97 used. The sternal and vertebral extremities were fixed, respectively, in an adjustable cardan joint to  
 98 the testing machine crosshead and in a ball-joint to the testing machine frame (Fig. 1). After the  
 99 alignment of the rib extremities to the loading axis of the testing machine, the ball-joint was locked  
 100 while the sternal extremity was left free for rotations around the transversal axis of the rib (cardan  
 101 joint). Each rib was preloaded at 5 N, to reduce the plays between the mechanical components of

102 the loading system, and a monotonic antero-posterior compression was applied, with a speed of 1  
103 mm/s, up to failure. Load and displacement were recorded by the computer of the testing machine  
104 at 100 Hz.



105

106 *Fig. 1: Illustration of the test setup. The ribs were compressed in antero-posterior direction using a*  
107 *uniaxial testing machine. The sternal extremity (anterior) of the ribs was fixed to an unconstrained*  
108 *cardan joint, whereas the vertebral extremity (posterior) was fixed to a locked ball-joint. A field of*  
109 *view of 100x30 mm was acquired by the two DIC cameras. Within the field of view, a region of*  
110 *interest (ROI) was defined at the 20% of the rib length from the sternal extremity. In the picture on*  
111 *the right, a region of interest (ROI) on the cutaneous surface is reported. A similar region of interest*  
112 *was defined on the pleural surface in those ribs with pleural field of view.*

113 The strain fields of the ribs were evaluated with a 3D-DIC (Q400, Dantec-Dynamics, Skovlunde,  
114 Denmark), synchronized with the testing machine. The system consisted of 2 cameras (5MPixels,  
115 2440x2050 pixels, 8-bit, black-and-white) with high-quality metrology-standard 35 mm lens  
116 (Xenoplan, Schneider-Kreuznach, Germany) and a directional system of LEDs (10'000 lumens in  
117 total). The hardware and software settings (Table 2) were optimized, similar to (Palanca et al., 2015,  
118 2018).

119 *Table 2: Summary of lens data and DIC parameters.*



DIC settings	Value
Aperture	f/16
Shutter time	1/50 s
Frame rate	10 Hz
Pixel size	0.03 mm
Facet size	25-39 pixels
Grid spacing	11-17 pixels
Filter	Kernel 9x9

120 In order to provide a complete characterization of the strain patterns on the ribs, 45 ribs were  
121 addressed for strain measurements on the cutaneous surface, while the other 44 were chosen for  
122 measurement on the pleural surface. A field of view of 100x30 mm, with a consequent pixel size of  
123 0.03 mm, was chosen to get a global quantitative description of the rib strain patterns. This field of  
124 view was chosen as a compromise between the spatial resolution, small enough to catch the local  
125 behavior of the rib (Palanca et al., 2015), and the framing, large enough to catch the rib fracture.  
126 In addition, medians of the principal strains were computed on a squared region of interest (ROI)  
127 within the DIC field of view for comparison between the different ribs. The ROI was localized at the  
128 20% of the rib length from the sternal extremity, with a dimension like the outer/inner cortex on  
129 the cutaneous/pleural field of view (Table 1), since fractures due to antero-posterior compression  
130 mostly happen in the anterior one third (Yang et al., 2011).

### 131 Assessment of bone quality and bone morphology

132 None of the specimens had signs of bony defects, fracture, or degeneration.  
133 The bone quality of the ribs was indirectly assessed evaluating the bone mineral density (BMD) of  
134 the respective spine in L2, L3 and L4 vertebral bodies by means of a quantitative computed  
135 tomography (Somatom Definition AS, Siemens Healthcare, Erlangen, Germany) with an integrated  
136 density-reference phantom (Osteo Phantom, Siemens Healthineers, Erlangen, Germany). According  
137 to the manufacturer's instructions, the spine was scanned with a voltage of 80 kVp and a current of  
138 105 mAs, obtaining a voxel size of 0.87x0.87x0.6 mm. The standardized software protocol  
139 segmented the trabecular bone of the L2, L3 and L4 vertebral bodies, averaged the attenuation  
140 values in Hounsfield Unit (HU) over the three vertebrae, and estimated the volumetric BMD through  
141 a HU-to-BMD conversion equation (Baum et al., 2011; Löffler et al., 2019).

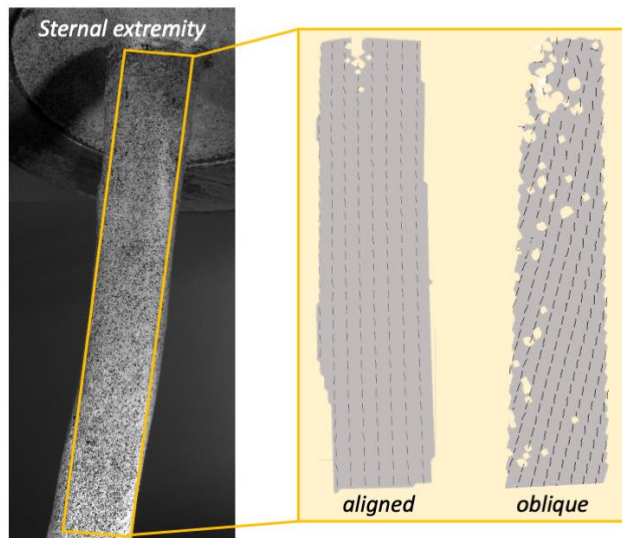
142 Micro-CT scans (Skyscan 1172 Micro-CT, Skyscan, Kontich, Belgium) were performed to evaluate the  
143 cortical thickness of each rib, in about 10 mm long samples cut posteriorly from the fracture site.  
144 The ribs were scanned with the following energetic parameters: 100 kVp, 100  $\mu$ As, with an Al-Cu  
145 filter, obtaining an isotropic voxel size of 5  $\mu$ m. The scanner manufacturer software CTAn (v  
146 1.17.7.2, Skyscan, Kontich, Belgien) was used for the microstructural analysis: the images were  
147 segmented using a standard single threshold approach for grayscale values in combination with a  
148 calibration phantom (Bruker MicroCT, Kontich, Belgium). The cortical thickness was measured on a  
149 volume of interest of 50 adjacent sample slices. For each slice, the average radial thickness (distance  
150 between the endosteum and periosteum surfaces) was measured. Then, the thickness value for the  
151 each rib was defined as the minimum thickness of the volume of interest.

152

## 153 Metrics and statistical analysis

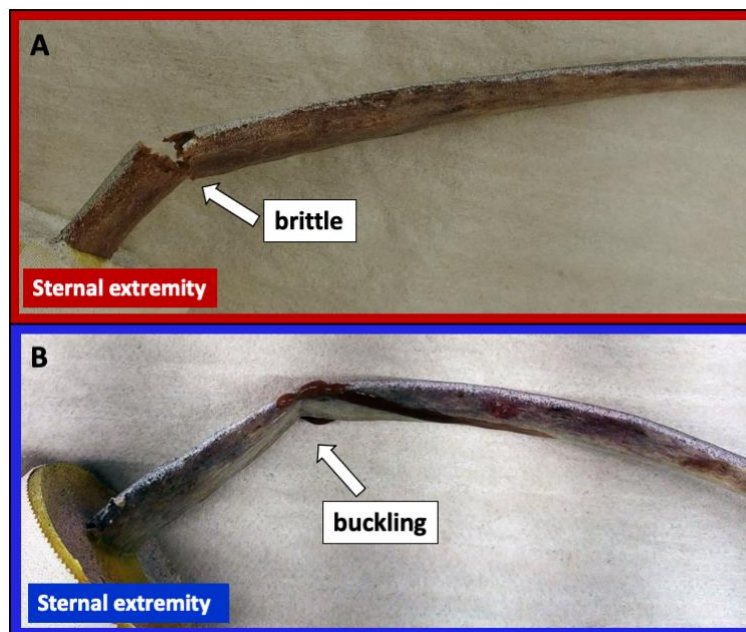
154 Each rib was mechanically characterized at fracture evaluating:

- 155 • the fracture load: the maximum force measured during the destructive test;
- 156 • the median of the maximum principal strain above the cutaneous/pleural ROI;
- 157 • the median of the minimum principal strain above the cutaneous/pleural ROI;
- 158 • the principal strain alignment above the field of view (Fig. 2): as the principal strains were  
159 either aligned close to the ribs axis, or approximately at 45°, the principal strain direction  
160 evaluated in the ROI was categorized either as “aligned” (when the average angle was  
161 smaller than 20° from the axis) or as “oblique” (when the average angle was in the range 20°  
162 - 45°);
- 163 • the mechanism of failure (Fig. 3), which was categorized into:
  - 164 ○ Brittle: the fracture was complete and sharp, with failure starting from the cutaneous  
165 surface due to tensile strain,
  - 166 ○ Buckling: the fracture was incomplete, and the rib behaved as a hollow pipe, with  
167 failure starting from the pleural surface due to compressive strain.



168

169 *Fig. 2: Principal strain direction was oriented in two distinct ways: aligned with the ribs or oblique,*  
 170 *around 45°, with respect to the rib.*



171

172 *Fig. 3: The two mechanisms of failure observed: brittle (A) and buckling (B).*

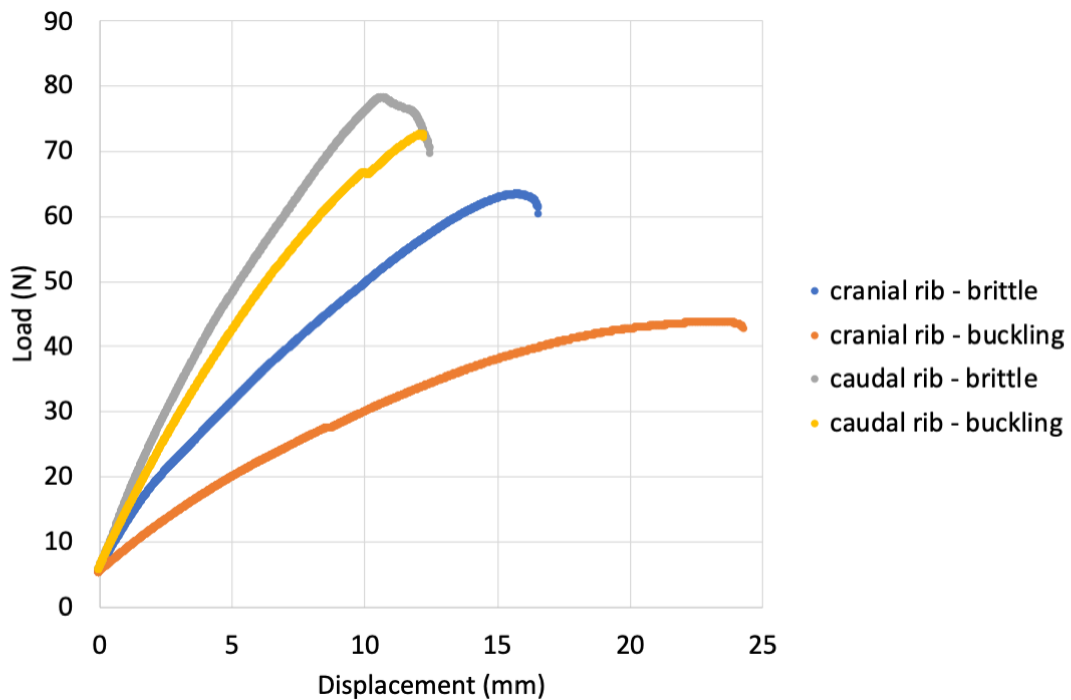
173 The correlations of the ribs levels with respect to the maximum principal strains and the minimum  
 174 principal strains were explored. Normality of the distributions was assessed with the Shapiro-Wilk  
 175 test. If data met the normality criterion ( $p > 0.05$ ), a parametric one-way ANOVA was performed,  
 176 followed by a Tukey's multiple comparison. Otherwise, a non-parametric Kruskal-Wallis test with a  
 177 Dunn's multiple comparison was applied.

178 The characterization was extended to the mechanism of failure mode and to the strain direction. To  
 179 evaluate if a mechanism of failure and a strain alignment were typical for a specific rib level, the Chi-

180 square test was used. In addition, as the ribs were categorized in terms of mechanism of failure  
181 (buckling or brittle) and of principal strain alignment (aligned or oblique), the possible association  
182 between mechanism of failure and strain alignment was assessed with the Fisher's exact test.  
183 Finally, the possible association of the mechanism of failure with the failure load, with the maximum  
184 principal strains, with the minimum principal strains, and with the cortical thickness in the  
185 retrospective failure section were explored. In the last case, due to the physiological differences in  
186 terms of ribs dimensions among the different levels of the ribs, a normalization of the rib cortical  
187 thickness was performed. The mean cortical thickness for each rib level was evaluated as the  
188 average of the cortical thickness in the closeness of the fracture among the ribs of such level. Then,  
189 the normalized cortical thickness was computed for each rib, as the ratio between the measured  
190 cortical thickness of that rib, and the mean cortical thickness at that level. The normality of  
191 distributions was tested with the Shapiro-Wilk test. If the sample passed the normality test, the  
192 association were tested with an unpaired t-test, otherwise a Mann-Whitney test was used to  
193 compare the ranks.  
194 All statistical analyses were performed with Prism 8 (GraphPad Software, USA), using a level of  
195 statistical significance at 0.05.

## 196 Results

197 All ribs showed a qualitatively similar load-displacement trend: quasi-linear in the initial phase and  
198 followed by a non-linear phase with decreasing slope, ending with an abrupt force drop (Fig. 4).



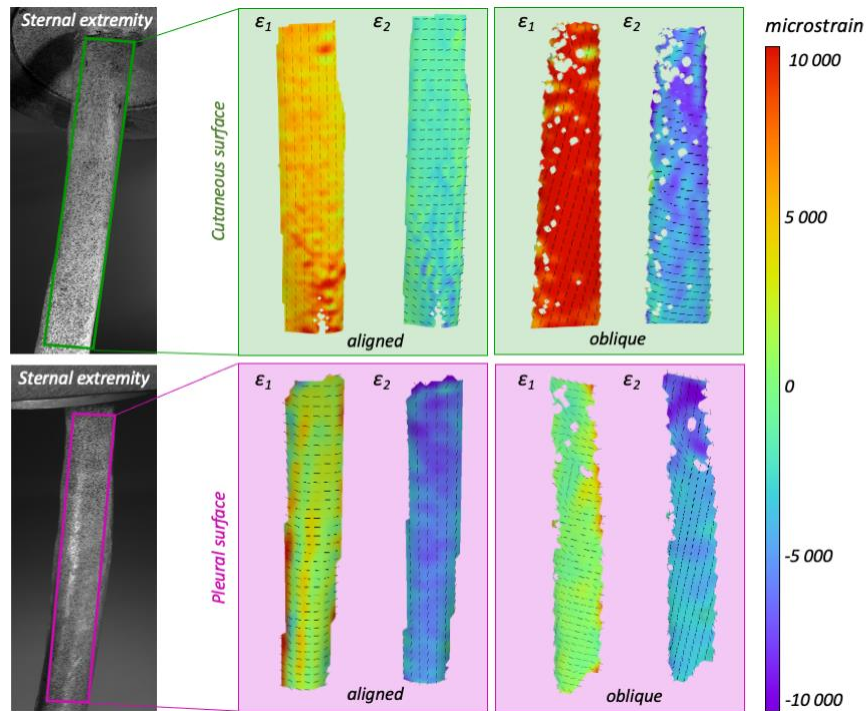
199

200 *Fig. 4: Typical load-displacement curves of cranial and caudal ribs with a brittle and buckling*  
 201 *mechanism of failure. The rib was pre-loaded at 5 N (initial point), then a monotonic compression*  
 202 *up to failure (force drop) was applied. In blue data from donor 3, rib 4 left; in orange data from donor*  
 203 *6, rib 4 left; in grey data from donor 3, rib 7 right; and in yellow data from donor 2, rib 7 left.*

204 The majority of the ribs showed simple fracture patterns (85/89), in particular 60 transverse and 25  
 205 oblique fractures, while the remaining 4 ribs showed multi-fragmentary fracture pattern, according  
 206 to the AO/OTA fracture classification (Meinberg et al., 2018). The onset fracture location in 88  
 207 out of 89 cases was in the 25% of the rib length from the sternal extremity, while just one specimen  
 208 fractured close to the vertebral extremity.

209 The fracture load ranged between 7.3 N (donor: 13, rib: 7 right) and 132 N (donor: 3, rib: 7 right),  
 210 with a coefficient of variation equal to 40% (SD/mean), as reported also in (Liebsch et al., 2021).

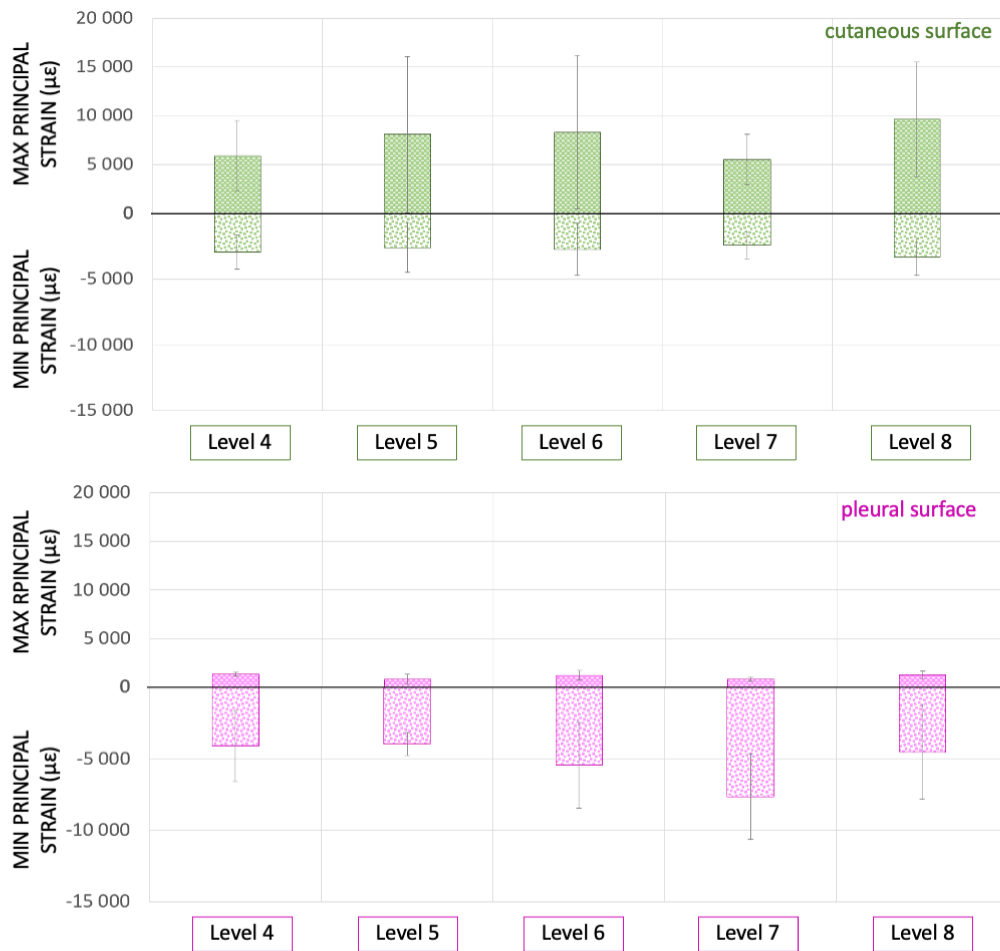
211 83 ribs (41 analyzed on the cutaneous surface and 42 analyzed on the pleural surface) were  
 212 considered for the strain analysis, 6 out of 89 ribs were excluded due to poor DIC correlation. The  
 213 analysis of the DIC-measured strains showed a systematic error of 20 microstrain and a random  
 214 error of 60 microstrain. The global quantitative characterization of the ribs showed a homogeneous  
 215 strain distribution, with no obvious strain concentrations, for both the cutaneous and pleural ROI,  
 216 for both the maximum and the minimum principal strain (Fig. 5). The direction of the principal  
 217 strains was aligned in 50 ribs and oblique in 31 ribs (Fig. S2). The principal strain direction was not  
 218 identified in two cases (donor: 10, rib: 4 right; donor: 12, rib: 5 right) which were excluded.



219

220 *Fig. 5: Maximum ( $\epsilon_1$ ) and minimum ( $\epsilon_2$ ) principal strains measured by the DIC on the field of view of*  
 221 *the cutaneous surface (top green boxes) and pleural surface (bottom purple boxes) of the ribs*  
 222 *immediately before failure. Each box represents a different rib. The dashes overlaid on the strain*  
 223 *maps show the direction of the principal strains: they were either roughly aligned with the rib*  
 224 *("aligned"), or at 45° ("oblique").*

225 The maximum principal strains above the ROI on the cutaneous surface ranged between 1000  
 226 microstrain (donor: 10, rib: 4 right) and 30000 microstrain (donor: 8, rib: 5 right), while on the  
 227 pleural surface it ranged between -3900 microstrain (donor: 12, rib: 7 right) and 2300 microstrain  
 228 (donor: 6, rib: 7 left). The minimum principal strains above the ROI on the cutaneous surface ranged  
 229 between -6200 microstrain (donor: 12, rib: 8 right) and -100 microstrain (donor: 9, rib: 7 left), while  
 230 on the pleural surface, it ranged between -30000 microstrain (donor: 9, rib: 7 right) and -800  
 231 microstrain (donor: 6, rib: 5 left)(Fig. 6).



232

233 *Fig. 6: Maximum and minimum principal strain measured by the DIC on the ROI of the cutaneous*  
 234 *surface (top, green) and on the pleural surface (bottom, purple) of the ribs immediately before*  
 235 *failure. The mean and standard deviations among the ribs at each level are plotted.*

236 Two mechanisms of failure were observed: the buckling mechanism (n=35/89), where collapse  
 237 initiated by inwards folding on the pleural cortex under compressive strains and the brittle  
 238 mechanism (n=42/89), where the collapse was clear-cut (Fig. 3). In twelve cases, the mechanism of  
 239 failure was not clear, because it resulted in a mix of the two principals.

240 No significant differences were observed for the principal strains at the different rib levels (Fig. 6)  
 241 (Kruskal-Wallis, see table 3 for the p-values).

242 No correlation existed between the mechanism of failure and the rib level (Chi-square test, p-value  
 243 = 0.492) as well as between the strain direction and the rib level (Chi-square test, p-value = 0.866).

244 No dichotomy existed between the mechanism of failure and the principal strain direction (Fig. S3,  
 245 Fisher's exact test, p-value = 0.639).

246 The fracture loads were similar in case of brittle or buckling mechanism of failure (Mann-Whitney  
 247 test, p-value = 0.136). The maximum principal strains on the cutaneous surface were significantly

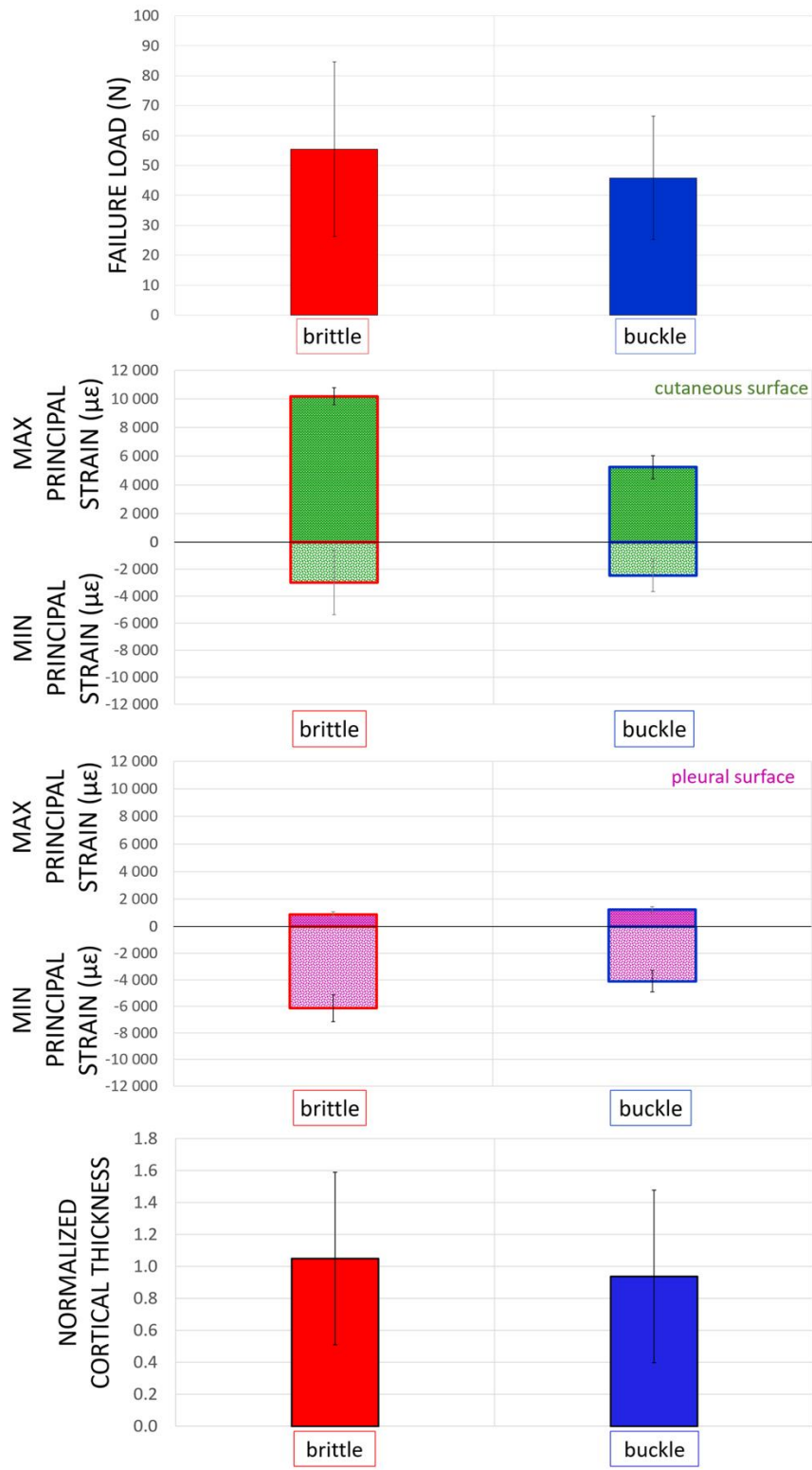
248 larger (Mann-Whitney test, p-value = 0.005) in the specimens failed with a brittle mechanism than  
 249 those with a buckle mechanism. By contrast, no trend was observed between the mechanism of  
 250 failure and the minimum principal strain (Mann-Whitney test, p-value = 0.700). No trends were  
 251 observed also between the mechanism of failure and the maximum and minimum principal strains  
 252 (Mann-Whitney test; respectively, p-value = 0.700 and p-value=0.140) on the pleural surface. The  
 253 specimens that fractured in brittle mechanism systematically showed thicker cortical layer  
 254 (unpaired t-test, p-value = 0.042) (Fig. 7 and Table 3).

255 *Table 3: Overview of the significance of the effects and correlations. The physical entities compared*  
 256 *are listed in the first column. The statistical test and the p-values are reported in the following*  
 257 *columns. The last column points to the illustration in the main paper or in the Supplementary*  
 258 *Material (SM) where each comparison can be found. The data for the statistical tests were collected*  
 259 *in the Supplementary Material (Table S1). Each sheet contains the data for each test reported in*  
 260 *Table 3.*

<b>Analysis</b>	<b>Statistical test</b>	<b>p-value</b>	<b>Figure</b>
Rib level vs eps max (cutaneous surface)	Kruskal-Wallis	0.431	Fig. 5
Rib level vs eps max (pleural surface)	Kruskal-Wallis	0.728	Fig. 5
Rib level vs eps min (cutaneous surface)	Kruskal-Wallis	0.705	Fig. 5
Rib level vs eps min (pleural surface)	Kruskal-Wallis	0.460	Fig. 5
Rib level vs mechanism of failure	Chi-square	0.492	SM, Fig. S1
Rib level vs strain direction	Chi-square	0.866	SM, Fig. S2
Mechanism of failure vs strain direction	Fisher's exact test	0.639	SM, Fig. S3
Mechanism of failure vs load	Mann-Whitney	0.136	Fig. 7
Mechanism of failure vs eps max (cutaneous surface)	Mann-Whitney	0.005 *	Fig. 7
Mechanism of failure vs eps max (pleural surface)	Mann-Whitney	0.700	Fig. 7
Mechanism of failure vs eps min (cutaneous surface)	Mann-Whitney	0.127	Fig. 7
Mechanism of failure vs eps min (pleural surface)	Mann-Whitney	0.140	Fig. 7
Mechanism of failure vs normalized cortical thickness	Unpaired t-test	0.042 *	Fig. 7

261 \* indicates statistical significance.





262  
 263 *Fig. 7: Failure load, maximum and minimum principal strain on the ROI of the cutaneous and*  
 264 *pleural surface, and normalized cortical thickness for the two mechanisms of failure (brittle and*  
 265 *buckling). The maximum principal strain on the cutaneous surface and the normalized cortical*  
 266 *thickness were systematically larger in those specimens that fractured in brittle mechanism.*

## 267 Discussion

268 The aim of this work was to provide a comprehensive characterization of the ribs in terms of failure  
269 load, mechanism of failure, and strain field at failure. We tested the hypothesis that correlations  
270 exist between global and local rib properties and the mechanism of failure.

271 A series of 89 ribs from 13 cadavers were tested in antero-posterior compression to replicate a  
272 fundamental component of the complex load which the ribs usually experience in case of severe  
273 thoracic compression (e.g. in cardio-pulmonary resuscitation or loading by occupant restraint  
274 systems).

275 Fracture patterns, load/displacement curves, and measured fracture loads were consistent with the  
276 ones showed by (Daegling et al., 2008; Yang et al., 2011), confirming the validity of this *in vitro*  
277 experiment. The fracture location, close to the sternal extremities, and the simple fracture pattern,  
278 with transverse and oblique fractures, replicated the fracture appearance observed in actual cases  
279 by (Harden et al., 2019). High variability in terms of fracture loads was found as a consequence of  
280 the different factors (i.e. rib morphology, bone mineral density) that (Liebsch et al., 2021) found  
281 leading to fracture. Nevertheless, homogeneous strain patterns with similar strain magnitudes  
282 were observed both in the cutaneous and pleural sides of the ribs. The strain patterns confirm the  
283 optimization of the rib structure for this loading scenario, as (Cristofolini, 2015) showed for other  
284 bones loaded in physiological conditions.

285 Two different strain directions (either aligned with the rib, or oblique around 45°) were observed  
286 on the surface of the ribs, while a clear correlation with other parameters was not found in the  
287 present study. We hypothesize that a torsion component was introduced in some ribs by the  
288 intrinsic shape of the ribs itself that leans the direction of the principal strains measured on the  
289 cutaneous or pleural surface.

290 Regardless of the fracture pattern, two different mechanisms of failure were observed. Statistically  
291 significant differences were found between the two mechanisms of failure in relation to the  
292 maximum principal strain on the cutaneous surface: the maximum principal strains on the  
293 cutaneous surface, immediately before failure, were significantly higher in the specimens that  
294 underwent brittle failure than in those with buckle. This confirmed the existence of the brittle and  
295 buckling mechanisms driven by two different mechanical events (Love and Symes, 2004). A possible  
296 explanation could be attributed to the combined effect of the cortical thickness and of the loading  
297 scenario which the ribs undergo. The brittle failure of the ribs seems to be regulated by the  
298 maximum principal strain, which typically happens in thick cortical bones (i.e. the medial and

299 medial-posterior sides of the femoral neck in physiological loading direction fail in tension like a  
300 brittle material) (Tang et al., 2018). By contrast, the buckling mechanism observed in thin cortical  
301 bones (i.e. the lateral cortex of the femoral neck, which is similar to the ribs' cortical thickness, in  
302 sideways fall condition fails in compression) seemed to be driven by cortical instability due to  
303 compressive stress. Analyses of the microcracking patterns could confirm at the microscale what  
304 we observed at the macroscale (Tang et al., 2018).

305 The failures of the ribs in tension region confirmed the different behaviour of the ribs with respect  
306 to other bones, as observed by (Love and Symes, 2004). This is highlighted also by the study of  
307 (Albert et al., 2021) on the ribs cortical tissue, which showed yield strains larger in compression  
308 than in tension, but ultimate strains smaller in compression than in tension, both for slow (i.e. 0.005  
309 strain/s) and fast (i.e. 0.5 strain/s) loading rate.

310 No significant difference in the fracture load was found between the groups with brittle and with  
311 buckling fracture. As explained in previous works, the cortical thickness plays a fundamental role in  
312 promoting rib fragility (Holcombe et al., 2019; Liebsch et al., 2021). In the present study, thin cortical  
313 thickness of the ribs loaded in antero-posterior direction induced buckling. This effect was  
314 confirmed by the significant difference between the cortical thickness of the ribs fractured in brittle  
315 mechanism (thicker) and the ones fractured in buckling mechanism (significantly thinner). In this  
316 respect, different loading conditions (i.e. the loads induced by automotive belt) may induce  
317 different mechanisms of failure.

318 To the authors' knowledge, a rationale to explain the two different mechanisms of failure of the rib  
319 was not developed yet and could be an interesting parameter to focus on in case of numerical  
320 modelling for forensic purposes. Indeed, several computational works reported the difficulty in  
321 accounting for the mechanism of failure (Iraeus et al., 2020; Li et al., 2010b, 2010a). The  
322 experimental evidence obtained in this work, as well as in (Liebsch et al., 2021), stresses the  
323 importance of the cortical thickness in the rib mechanism of failure. This supports the application  
324 of dedicated numerical tools (Iraeus et al., 2020, 2019), as the cortical bone mapping (Holcombe et  
325 al., 2018), to better discriminate the cortical thickness also from clinical CT images. A simplified  
326 evaluation of the cortical thickness may be sufficient, instead, if the aim is to estimate the fracture  
327 load or the strain field (Li et al., 2010a).

328 The loading condition implemented in the present study was a simplification compared with the  
329 complex loading conditions experienced during a high-energy trauma or a fall. However, although  
330 antero-posterior compression is not the one and only load component acting on the ribs, it is one

331 of the most relevant components (Liebsch et al., 2019a). Furthermore, as traumatic events are  
332 highly variable and scarcely predictable, it would be impossible to define a unique complex loading  
333 scenario. For this reason, a simplified one, yet based on the predominant component of load was  
334 chosen, as it is most reproducible. Another limitation of this study could be the relatively low loading  
335 rate compared to the loading rate of an actual trauma (Katzenberger et al., 2020). However, the  
336 loading rate was chosen to enable accurate strain measurement with DIC. Larger strains could be  
337 expected in case of increased loading rate (Albert et al., 2021). However, the loading rate is not  
338 likely to have affected the overall findings of the study.

## 339 Conclusions

340 The experimental tests performed on a large sample of ribs allowed to replicate clinically relevant  
341 fracture patterns. In particular, the tests confirmed the existence of two specific mechanisms of  
342 failure, brittle and buckling. The maximum principal strain field associated with the two mechanisms  
343 of failure were significantly different. We showed evidence of the importance of the cortical  
344 thickness driving either a brittle or buckling mechanism of failure in the human ribs.

## Acknowledgements

This study was funded by the German Research Foundation (DFG, project WI 1352/20-2).

## References

- Agnew, A., Moorhouse, K., Murach, M., White, S., Kang, Y.-S., 2014. Tensile stress in human ribs throughout the lifespan. IRCOBI conference 2014.
- Albert, D.L., Katzenberger, M.J., Agnew, A.M., Kemper, A.R., 2021. A comparison of rib cortical bone compressive and tensile material properties: Trends with age, sex, and loading rate. *Journal of the Mechanical Behavior of Biomedical Materials* 122, 104668. <https://doi.org/10.1016/j.jmbbm.2021.104668>
- Baum, T., Müller, D., Dobritz, M., Rummeny, E.J., Link, T.M., Bauer, J.S., 2011. BMD measurements of the spine derived from sagittal reformations of contrast-enhanced MDCT without dedicated software. *European Journal of Radiology* 80, e140–e145. <https://doi.org/10.1016/j.ejrad.2010.08.034>
- Bayraktar, H.H., Morgan, E.F., Niebur, G.L., Morris, G.E., Wong, E.K., Keaveny, T.M., 2004. Comparison of the elastic and yield properties of human femoral trabecular and cortical bone tissue. *Journal of Biomechanics* 37, 27–35. [https://doi.org/10.1016/S0021-9290\(03\)00257-4](https://doi.org/10.1016/S0021-9290(03)00257-4)
- Brasel, K.J., Guse, C.E., Layde, P., Weigelt, J.A., 2006. Rib fractures: Relationship with pneumonia and mortality\*: *Critical Care Medicine* 34, 1642–1646. <https://doi.org/10.1097/01.CCM.0000217926.40975.4B>
- Campbell, N., Conaglen, P., Martin, K., Antippa, P., 2009. Surgical Stabilization of Rib Fractures Using Inion OTPS Wraps—Techniques and Quality of Life Follow-Up. *Journal of Trauma: Injury, Infection & Critical Care* 67, 596–601. <https://doi.org/10.1097/TA.0b013e3181ad8cb7>
- Cristofolini, L., 2015. In vitro evidence of the structural optimization of the human skeletal bones. *Journal of Biomechanics* 48, 787–796. <https://doi.org/10.1016/j.jbiomech.2014.12.010>
- Daegling, D.J., Warren, M.W., Hotzman, J.L., Self, C.J., 2008. Structural Analysis of Human Rib Fracture and Implications for Forensic Interpretation\*. *Journal of Forensic Sciences*. <https://doi.org/10.1111/j.1556-4029.2008.00876.x>
- Duma, S.M., Kemper, A.R., Stitzel, J.D., McNally, C., Kennedy, E.A., Matsuoka, F., 2011. Rib fracture timing in dynamic belt tests with human cadavers. *Clin. Anat.* 24, 327–338. <https://doi.org/10.1002/ca.21130>
- Harden, A., Kang, Y.-S., Agnew, A., 2019. Rib Fractures: Validation of an Interdisciplinary Classification System. *fa* 2, 158–167. <https://doi.org/10.5744/fa.2019.1032>
- Harden, A., Kang, Y.-S., Moorhouse, K., Agnew, A., 2017. Variance in Fracture Location of Human Ribs Subjected to Dynamic Antero-Posterior Bending. IRCOBI conference 2017.
- Holcombe, S.A., Hwang, E., Derstine, B.A., Wang, S.C., 2018. Measuring rib cortical bone thickness and cross section from CT. *Medical Image Analysis* 49, 27–34. <https://doi.org/10.1016/j.media.2018.07.003>
- Holcombe, S.A., Kang, Y., Derstine, B.A., Wang, S.C., Agnew, A.M., 2019. Regional maps of rib cortical bone thickness and cross-sectional geometry. *J. Anat.* 235, 883–891. <https://doi.org/10.1111/joa.13045>
- Iraeus, J., Brolin, K., Pipkorn, B., 2020. Generic finite element models of human ribs, developed and validated for stiffness and strain prediction – To be used in rib fracture risk evaluation for the human population in vehicle crashes. *Journal of the Mechanical Behavior of Biomedical Materials* 106, 103742. <https://doi.org/10.1016/j.jmbbm.2020.103742>
- Iraeus, J., Lundin, L., Storm, S., Agnew, A., Kang, Y.-S., Kemper, A., Albert, D., Holcombe, S., Pipkorn, B., 2019. Detailed subject-specific FE rib modeling for fracture prediction. *Traffic Injury Prevention* 20, S88–S95. <https://doi.org/10.1080/15389588.2019.1665649>

- Kang, Y.-S., Kwon, H.J., Stammen, J., Moorhouse, K., Agnew, A.M., 2021. Biomechanical Response Targets of Adult Human Ribs in Frontal Impacts. *Ann Biomed Eng* 49, 900–911. <https://doi.org/10.1007/s10439-020-02613-x>
- Katzenberger, M.J., Albert, D.L., Agnew, A.M., Kemper, A.R., 2020. Effects of sex, age, and two loading rates on the tensile material properties of human rib cortical bone. *Journal of the Mechanical Behavior of Biomedical Materials* 102, 103410. <https://doi.org/10.1016/j.jmbbm.2019.103410>
- Keaveny, T.M., Guo, X.E., Wachtel, E.F., McMahon, T.A., Hayes, W.C., 1994. Trabecular bone exhibits fully linear elastic behavior and yields at low strains. *Journal of Biomechanics* 27, 1127–1136. [https://doi.org/10.1016/0021-9290\(94\)90053-1](https://doi.org/10.1016/0021-9290(94)90053-1)
- Kemper, A., McNally, C., Pullins, C., Freeman, L., Duma, S., Rouhana, S., 2007. The biomechanics of human ribs: Material and structural properties from dynamic tension and bending tests. *Stapp car crash journal* 51, 235–73.
- Kent, R., Woods, W., Bostrom, O., 2008. Fatality Risk and the Presence of Rib Fractures. *Proceedings of advances in automotive medicine* 52, 73.
- Li, Z., Kindig, M.W., Kerrigan, J.R., Untaroiu, C.D., Subit, D., Crandall, J.R., Kent, R.W., 2010a. Rib fractures under anterior–posterior dynamic loads: Experimental and finite-element study. *Journal of Biomechanics* 43, 228–234. <https://doi.org/10.1016/j.jbiomech.2009.08.040>
- Li, Z., Kindig, M.W., Subit, D., Kent, R.W., 2010b. Influence of mesh density, cortical thickness and material properties on human rib fracture prediction. *Medical Engineering & Physics* 32, 998–1008. <https://doi.org/10.1016/j.medengphy.2010.06.015>
- Liebsch, C., Graf, N., Wilke, H.-J., 2019a. In vitro analysis of kinematics and elastostatics of the human rib cage during thoracic spinal movement for the validation of numerical models. *Journal of Biomechanics* 94, 147–157. <https://doi.org/10.1016/j.jbiomech.2019.07.041>
- Liebsch, C., Hübner, S., Palanca, M., Cristofolini, L., Wilke, H.-J., 2021. Experimental study exploring the factors that promote rib fragility in the elderly. *Sci Rep* 11, 9307. <https://doi.org/10.1038/s41598-021-88800-9>
- Liebsch, C., Seiffert, T., Vlcek, M., Beer, M., Huber-Lang, M., Wilke, H.-J., 2019b. Patterns of serial rib fractures after blunt chest trauma: An analysis of 380 cases. *PLoS ONE* 14, e0224105. <https://doi.org/10.1371/journal.pone.0224105>
- Liebsch, C., Wilke, H.-J., 2018. Chapter 3 - Basic Biomechanics of the Thoracic Spine and Rib Cage, in: Galbusera, F., Wilke, H.-J. (Eds.), *Biomechanics of the Spine*. Academic Press, pp. 35–50. <https://doi.org/10.1016/B978-0-12-812851-0.00003-3>
- Lionello, G., Cristofolini, L., 2014. A practical approach to optimizing the preparation of speckle patterns for digital-image correlation. *Measurement Science and Technology* 25, 107001. <https://doi.org/10.1088/0957-0233/25/10/107001>
- Löffler, M.T., Jacob, A., Valentinitich, A., Rienmüller, A., Zimmer, C., Ryang, Y.-M., Baum, T., Kirschke, J.S., 2019. Improved prediction of incident vertebral fractures using opportunistic QCT compared to DXA. *Eur Radiol* 29, 4980–4989. <https://doi.org/10.1007/s00330-019-06018-w>
- Love, J.C., Symes, S.A., 2004. Understanding Rib Fracture Patterns: Incomplete and Buckle Fractures. *J. Forensic Sci.* 49, 1–6. <https://doi.org/10.1520/JFS2004175>
- Meinberg, E., Agel, J., Roberts, C., Karam, M., Kellam, J., 2018. Fracture and Dislocation Classification Compendium—2018. *Journal of Orthopaedic Trauma* 32, S1–S10. <https://doi.org/10.1097/BOT.0000000000001063>
- Mohr, M., Abrams, E., Engel, C., Long, W.B., Bottlang, M., 2007. Geometry of human ribs pertinent to orthopedic chest-wall reconstruction. *Journal of Biomechanics* 40, 1310–1317. <https://doi.org/10.1016/j.jbiomech.2006.05.017>

- Nirula, R., Mayberry, J.C., 2010. Article Commentary: Rib Fracture Fixation: Controversies and Technical Challenges. *The American Surgeon* 76, 793–802. <https://doi.org/10.1177/000313481007600820>
- Palanca, M., Brugo, T.M.M., Cristofolini, L., 2015. Use of Digital Image Correlation to Understand the Biomechanics of the Vertebra. *Journal of Mechanics in Medicine and Biology* 15, 1540004–1540010. <https://doi.org/10.1142/S0219519415400047>
- Palanca, M., Marco, M., Ruspi, M.L., Cristofolini, L., 2018. Full-field strain distribution in multi-vertebra spine segments: An in vitro application of digital image correlation. *Medical Engineering & Physics* 52, 76–83. <https://doi.org/10.1016/j.medengphy.2017.11.003>
- Pezowicz, C., Glowacki, M., 2021. The mechanical properties of human ribs in young adult. *Acta of Bioengineering and Biomechanics* 14, 53–50.
- Reilly, D.T., Burstein, A.H., 1975. The elastic and ultimate properties of compact bone tissue. *Journal of Biomechanics* 8, 393–405. [https://doi.org/10.1016/0021-9290\(75\)90075-5](https://doi.org/10.1016/0021-9290(75)90075-5)
- Tang, T., Crompton, P.A., Guy, P., McKay, H.A., Wang, R., 2018. Clinical hip fracture is accompanied by compression induced failure in the superior cortex of the femoral neck. *Bone* 108, 121–131. <https://doi.org/10.1016/j.bone.2017.12.020>
- Wang, F., Yang, J., Miller, K., Li, G., Joldes, G.R., Doyle, B., Wittek, A., 2016. Numerical investigations of rib fracture failure models in different dynamic loading conditions. *Computer Methods in Biomechanics and Biomedical Engineering* 19, 527–537. <https://doi.org/10.1080/10255842.2015.1043905>
- Yang, K., Lynch, M., O'Donnell, C., 2011. “Buckle” rib fracture: An artifact following cardio-pulmonary resuscitation detected on postmortem CT. *Legal Medicine* 13, 233–239. <https://doi.org/10.1016/j.legalmed.2011.05.004>
- Yoganandan, N., Pintar, F.A., 1998. Biomechanics of Human Thoracic Ribs. *Journal of Biomechanical Engineering* 120, 100–104. <https://doi.org/10.1115/1.2834288>



Supplementary materials:

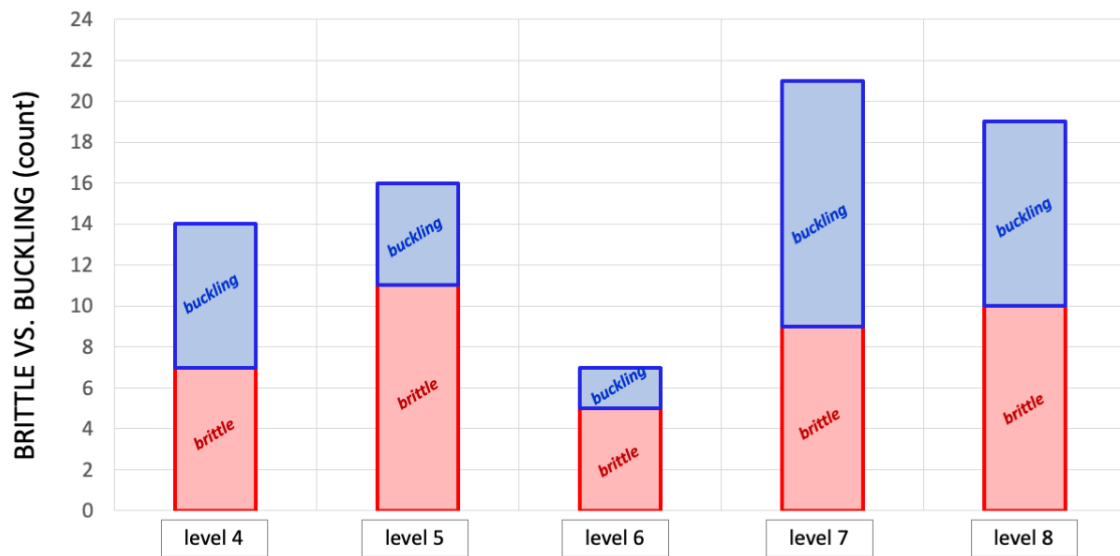


**Fig. S1.** Different mechanisms of fracture (brittle vs buckling) for the single rib levels. The red columns represent the count of the ribs fractured in brittle mode while the blue columns represent the ribs fractured in buckle mode.

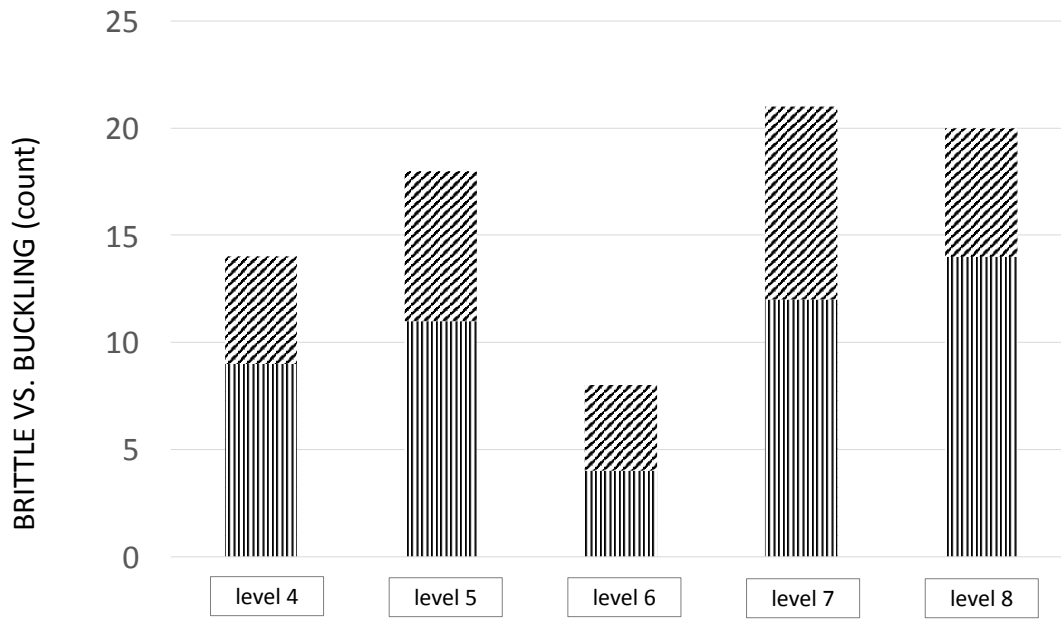


**Fig. S2.** Different principal strain directions (aligned vs oblique) for the single rib levels. The columns with the aligned pattern represent the ribs with aligned principal strain direction, while the columns with the oblique pattern represent the ribs with oblique principal strain direction.

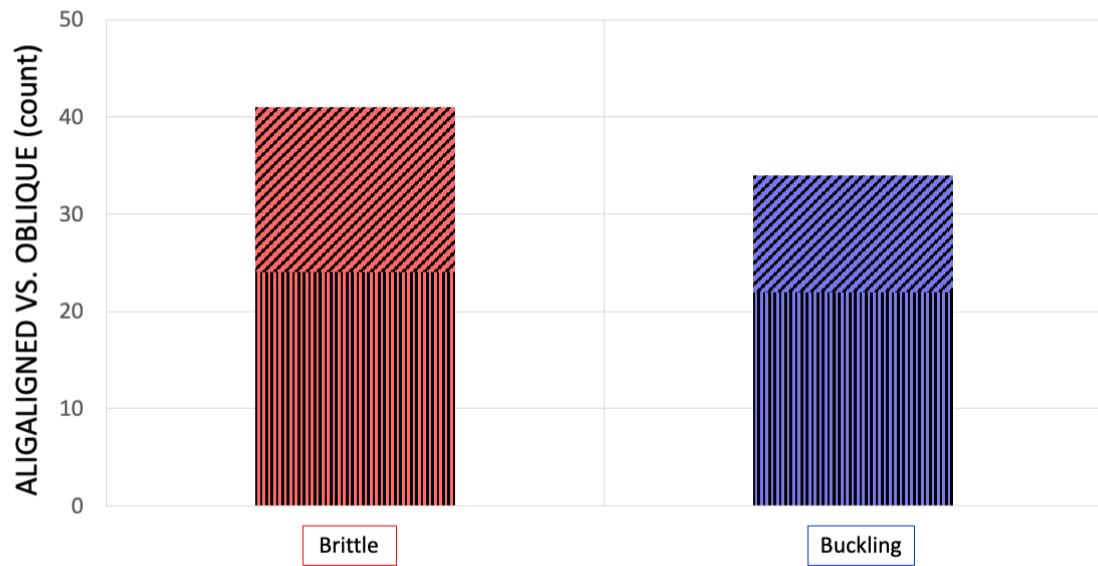


**Fig. S3.** Binning of the mechanisms of failure with respect to the principal strain direction. The red column represents the ribs that fractured in brittle mode while the blue column represents the ribs that fractured in buckling mode. Each column was divided in the proportion of ribs with aligned principal strain direction (aligned pattern of the column) and the ribs with the oblique principal strain direction (oblique pattern of the column).

**Table S1.**

Data used for the statistical analysis reported in Table 3 of the main text.

Each sheet contains the data for the comparison between the reported physical entities (column 'Analysis' of Table 3 of the main text).